Human Neuroblasts Migrate to the Olfactory Bulb via a Lateral Ventricular Extension

Maurice A. Curtis, *et al.*

Science **315**, 1243 (2007);
DOI: 10.1126/science.1136281

Science (print ISSN 0036-8075; online ISSN 1095-9203) is published weekly, except the last week in December, by the American Association for the Advancement of Science, 1200 New York Avenue NW, Washington, DC 20005.

It is uncontroversial to postulate direct observations of the annual movement of the rising or setting Sun along the horizon for the purposes of regulating seasonal events such as religious festivals or for maintaining a seasonal calendar. Nonetheless, it is not simple to evaluate the nature of the observations made and the social and ritualistic context within which they operated and derived their relevance. This point is well illustrated by recent debates concerning the function of the so-called E-group structures in the Mayan heartlands of the Peten in Guatemala (*25*–*27*). In the case of the Thirteen Towers and nearby plazas, we can infer that they provided a setting for people participating in public rituals and feasts directly linked to the observation and interpretation of the seasonal passage of the Sun. By contrast, entry to the observing points themselves appears to have been highly restricted. Individuals with the status to access them and conduct ceremonies would have had the power to regulate time, ideology, and the rituals that bound this society together. Additionally, the excavations at Chankillo have uncovered ceramic warrior figurines holding a great variety of offensive (and defensive) weapons (*14*) (fig. S5). The warriors depicted wear signs of distinction, such as headdresses, shirts, and especially neck, chest, and nose ornaments. The artistic representation of these warriors, holding specialized weapons and wearing the symbols of their high status, indicates the possible rise of a class of war leaders and the centralization of power and authority in the hands of a few. Thus, Sun worship and related cosmological beliefs at Chankillo could have helped to legitimize the authority of an elite class, just as they did within the Inca empire two millennia later. And this, in turn, implies that the towers were not a simple instrument for solar observation but the monumental expression of existing—and therefore by implication even older—knowledge.

There is increasing evidence that the Sun cult, which, as the official cult of the Inca empire, regulated calendrical ceremonies and supported the established social hierarchy, had precursors. For example, historically attested sunrise ceremonies at a sanctuary on the Island of the Sun in Lake Titicaca (*28*), surrounding a crag regarded as the origin place of the Sun, almost certainly had pre-Incaic roots (*29*). Given the similarity between the solar observation device at Chankillo and the Cusco pillars documented some two millennia later (*12*), it seems likely that similar practices were common within many of the great states that developed in the Andes before, as well as including, the Inca empire.

References and Notes

1. C. L. N. Ruggles, in *Archaeology: The Key Concepts*, A. C. Renfrew, P. G. Bahn, Eds. (Routledge, New York, 2005), pp. 11–16.
2. C. L. N. Ruggles, *Ancient Astronomy: An Encyclopedia of Cosmologies and Myth* (ABC-CLIO, Santa Barbara, CA, 2005).
3. A. F. Aveni, *Skywatchers* (Univ. of Texas Press, Austin, 2001), pp. 55–67.
4. Not all accurate sky-based seasonal calendars rely on horizon observations of the Sun: One exception is the traditional calendar of the Borana of Ethiopia and Kenya [M. Bassi, *Curr. Anthropol.* **29**, 619 (1988)], which is luni-stellar.
5. S. C. McCluskey, *J. Hist. Astron.* **8**, 174 (1977).
6. A. F. Aveni, H. Hartung, *Trans. Am. Phil. Soc.* **76**, 1 (1986).
7. I. Šprajc, *Orientaciones Astronómicas en la Arquitectura Prehispánica del Centro de México* (Instituto Nacional de Antropología e Historia, México Distrito Federal (D.F.), 2001).
8. M. S. Ziółkowski, R. M. Sadowski, Eds., *Time and Calendars in the Inca Empire* (British Archaeological Reports International Series, Oxford, 1989), vol. 479.
9. B. S. Bauer, D. S. P. Dearborn, *Astronomy and Empire in the Ancient Andes* (Univ. of Texas Press, Austin, 1995).
10. R. T. Zuidema, *The Ceque System of Cuzco: The Social Organization of the Capital of the Inca* (Brill, Leiden, Netherlands, 1964).
11. A. F. Aveni, *Stairways to the Stars* (Wiley, New York, 1997), pp. 147–176.
12. B. S. Bauer, *The Sacred Landscape of the Inca: The Cusco Ceque System* (Univ. of Texas Press, Austin, 1998).
13. B. S. Bauer, D. S. P. Dearborn, *Astronomy and Empire in the Ancient Andes* (Univ. of Texas Press, Austin, 1995), pp. 67–100.
14. I. Ghezzi, in *Andean Archaeology III: North and South*, W. Isbell, H. Silverman, Eds. (Springer, New York, 2006), pp. 67–84.
15. J. R. Topic, T. L. Topic, in *Arqueologia, Antropologia e Historia en los Andes: Homenaje a Maria Rostworowski*, R. Varon, J. Flores, Eds. (Instituto de Estudios Peruanos, Lima, 1997), pp. 567–590.
16. I. Ghezzi, *Proyecto Arqueológico Chankillo: Informe de la Temporada 2003* (Instituto Nacional de Cultura, Lima, 2004).
17. C. L. N. Ruggles, *Astronomy in Prehistoric Britain and Ireland* (Yale Univ. Press, New Haven, CT, 1999), pp. ix.
18. C. L. N. Ruggles, *Astronomy in Prehistoric Britain and Ireland* (Yale Univ. Press, New Haven, CT, 1999), pp. 18, 24, and 57.
19. C. L. N. Ruggles, *J. Hist. Astron.* **28** (suppl. 22), S45 (1997).
20. A. F. Aveni, *Skywatchers* (Univ. of Texas Press, Austin, 2001), pp. 40–46 and 265–269.
21. R. T. Zuidema, in *Archaeoastronomy in the Americas*, R. A. Williamson, Ed. (Ballena, Los Altos, CA, 1981), pp. 319–342.
22. B. S. Bauer, D. S. P. Dearborn, *Astronomy and Empire in the Ancient Andes* (Univ. of Texas Press, Austin, 1995), pp. 94–98.
23. C. L. N. Ruggles, *Astronomy in Prehistoric Britain and Ireland* (Yale Univ. Press, New Haven, CT, 1999), pp. 91–111.
24. M. A. Hoskin, *Tombs, Temples and Their Orientations* (Ocarina Books, Bognor Regis, UK, 2001).
25. A. F. Aveni, H. Hartung, in *World Archaeastronomy*, A. F. Aveni, Ed. (Cambridge Univ. Press, Cambridge, 1989), pp. 441–461.
26. A. F. Aveni, A. S. Dowd, B. Vining, *Latin Am. Antiq.* **14**, 159 (2003).
27. G. R. Aylesworth, *Archaeoastronomy* **18**, 34 (2004).
28. B. S. Bauer, C. Stanish, *Ritual and Pilgrimage in the Ancient Andes: The Islands of the Sun and the Moon* (Univ. of Texas Press, Austin, 2001).
29. D. S. P. Dearborn, M. T. Seddon, B. S. Bauer, *Latin Am. Antiq.* **9**, 240 (1998).
30. C. Bronk Ramsey, *Radiocarbon* **37**, 425 (1995).
31. C. Bronk Ramsey, *Radiocarbon* **43**, 355 (2001).
32. F. G. McCormac *et al.*, *Radiocarbon* **46**, 1087 (2004).

33. We thank the numerous archaeologists and volunteers who participated in the Chankillo project, and especially J. L. Pino. We also thank Yale University, the Pontificia Universidad Católica del Peru, NSF, the Wenner-Gren Foundation, the Field Museum, the Schwerin Foundation, and Earthwatch Institute for support, as well as the Asociación Cultural Peruano Británica in Lima, Peru, for logistical and financial support. R. Towner and K. Anchukaitis were instrumental in securing five samples for dendrochronological dating. The warrior figurines were restored by Futuro Anterior. NSF funded all Accelerator Mass Spectrometry radiocarbon dates. I.G. is director of archaeology at the Instituto Nacional de Cultura.

Supporting Online Material

www.sciencemag.org/cgi/content/full/315/5816/1239/DC1
Materials and Methods
SOM Text
Figs. S1 to S5
Tables S1 to S4
References and Notes

17 October 2006; accepted 21 December 2006
10.1126/science.1136415

Human Neuroblasts Migrate to the Olfactory Bulb via a Lateral Ventricular Extension

Maurice A. Curtis,[1,2] Monica Kam,[1] Ulf Nannmark,[3] Michelle F. Anderson,[2] Mathilda Zetterstrom Axell,[2] Carsten Wikkelso,[2] Stig Holtås,[4] Willeke M. C. van Roon-Mom,[1] Thomas Björk-Eriksson,[5] Claes Nordborg,[6] Jonas Frisén,[7] Michael Dragunow,[8] Richard L. M. Faull,[1]* Peter S. Eriksson[2]*

The rostral migratory stream (RMS) is the main pathway by which newly born subventricular zone cells reach the olfactory bulb (OB) in rodents. However, the RMS in the adult human brain has been elusive. We demonstrate the presence of a human RMS, which is unexpectedly organized around a lateral ventricular extension reaching the OB, and illustrate the neuroblasts in it. The RMS ensheathing the lateral olfactory ventricular extension, as seen by magnetic resonance imaging, cell-specific markers, and electron microscopy, contains progenitor cells with migratory characteristics and cells that incorporate 5-bromo-2′-deoxyuridine and become mature neurons in the OB.

In the rodent brain, the RMS contains progenitor cells that migrate from the subventricular zone (SVZ), adjacent to the lateral ventricle, out to the OB. The RMS takes a course rostral to the striatum, and then the cells migrate forward in the olfactory tract to the OB. The human forebrain follows the basic structural organization of the mammalian brain but is extensively developed compared with that of rodents. The human OB, and hence the olfactory interneuron replacement

system, is comparatively smaller than that in rodents and is anatomically organized differently; therefore, the RMS has remained elusive in the human brain.

Many species possess an open tube between the lateral ventricle and olfactory ventricle, and this allows the free flow of cerebrospinal fluid (CSF) as well as a continuous SVZ between the two regions (*1*, *2*). This structure has not been previously shown in the human brain.

In the present study, we provide a characterization of the human ventriculo-olfactory neurogenic system (VONS) containing the SVZ, the RMS, the olfactory tract, and the OB. We demonstrate that the human RMS is organized around a lateral ventricular extension reaching the OB.

The anatomical location of the RMS in the human brain. Analysis of proliferating cell nuclear antigen (PCNA)–stained sagittal human forebrain sections (counterstained with Nissl) showed the presence of an RMS-like pathway. Proliferating cells were observed from the SVZ adjacent to the lateral ventricle overlying the caudate nucleus (CN) to the olfactory tract in the base of the forebrain (Fig. 1, A and B). A cleft in the floor of the anterior horn of the lateral ventricle contained large numbers of PCNA-positive cells that were continuous with the PCNA-positive cells in the SVZ that overlie the CN. The stream of cells first takes a caudal and ventral track along the undersurface of the CN, caudal to the genu of the corpus callosum and the frontal cortical white matter of the gyrus rectus (Fig. 1, A to D). When the descending limb reaches the ventral CN, the stream takes a rostral turn to form the rostral limb of the RMS that passes ventrally and rostrally to enter the anterior olfactory cortex (AOC), which gives rise to the olfactory tract that leads to the OB (Fig. 1A). Near the SVZ, more than 20 serial sagittal sections extending mediolaterally over 2.1 mm had PCNA-positive cells evident in the descending limb; at the level of the rostral limb, proliferating cells only extended mediolaterally over 0.6 mm. Thus, the overall mediolateral extent of the RMS is 2.7 mm from the SVZ to the olfactory tract, and the total length of the RMS pathway from the SVZ to the start of the olfactory tract is about 17 mm. High-magnification photomicrographs revealed the specific nuclear localization of the PCNA protein at the funnel where the RMS begins (Fig. 1E), in the decending limb (Fig. 1F), and in the rostral limb (Fig. 1G).

Serial coronal PCNA-stained sections revealed that the RMS takes a path from medial, by the SVZ, to lateral, beneath the CN; close to the SVZ the RMS is very wide in the coronal plane (Fig. 2, A and B). Coronal sections taken from the AOC region revealed two small oval bundles of PCNA-positive cells; the more dorsal bundle represented the descending limb of the RMS, and the more ventral bundle, the rostral limb of the RMS (Fig. 2C). Total cell counts throughout the entire lengths of the descending limb and the rostral limb of the RMS conducted on three cases showed that the RMS comprised 108,300 ± 13,310 cells (mean ± SD). Over 90% of the PCNA-positive cells were present in the descending limb and under 10% in the rostral limb, suggesting differentiation and dispersal along the stream (Fig. 2C). In the core of the olfactory tract, PCNA labeling formed a flat band. PCNA-labeled cells were present in the olfactory tract throughout its extension from the caudal region near the AOC (Fig. 2D) to the rostral extent, where the olfactory tract enters the OB.

Cell death is not the fate of most of the RMS progenitor cells. To examine whether PCNA was being expressed in the RMS cells because of DNA repair or apoptosis and not proliferation (*3*), we performed terminal deoxynucleotidyl transferase–mediated deoxyuridine triphosphate nick end labeling (TUNEL) to detect DNA fragmentation. No TUNEL was present in the descending limb of the RMS despite the presence of many TUNEL-positive cells in the adjacent CN (fig. S1).

Progenitors in the RMS have migratory proteins and a migratory morphology. Immunostaining for polysialylated–neural cell adhesion molecule (PSA-NCAM), which is expressed by migrating cells in the rodent RMS (*4*, *5*), was investigated in the SVZ near the cleft, the descending and rostral limbs of the RMS, the olfactory tract core and periphery, and the OB. In each region examined, PSA-NCAM–positive

[1]Department of Anatomy with Radiology, Faculty of Medical and Health Sciences, University of Auckland, Private Bag 92019, Auckland, New Zealand. [2]Center for Brain Repair and Rehabilitation, Institute of Neuroscience and Physiology, Sahlgrenska Academy, Medicinaregatan 11, Box 432, SE 405 30 Göteborg, Sweden. [3]Institute of Biomedicine at Sahlgrenska Academy, Medicinaregatan 11, Box 432, SE 405 30 Göteborg, Sweden. [4]Department of Radiology, Bruna Stråket 11 plan 2, Sahlgrenska University Hospital, SE 413 45 Göteborg, Sweden. [5]Department of Oncology, Sahlgrenska University Hospital, 413 45 Göteborg, Sweden. [6]Department of Pathology, Sahlgrenska University Hospital, 413 45 Göteborg, Sweden. [7]Department of Cell and Molecular Biology, Medical Nobel Institute, Karolinska Institute, SE-171 77 Stockholm, Sweden. [8]Department of Pharmacology, Faculty of Medical and Health Sciences, University of Auckland, Private Bag 92019, Auckland, New Zealand.

*To whom correspondence should be addressed. E-mail: per@neuro.gu.se (P.S.E.); rlm.faull@auckland.ac.nz (R.L.M.F.)

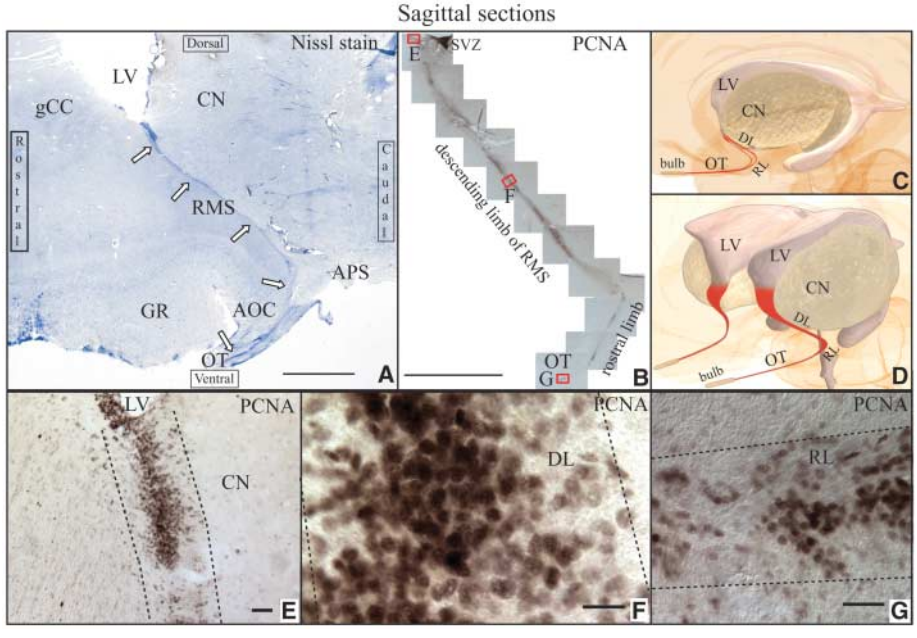

Fig. 1. The human RMS takes a caudal path en route from the SVZ to the olfactory cortex. (**A**) Nissl staining of human serial sagittal human forebrain sections reveals the intense stained cells that delineate the path of the RMS behind the frontal cortex white matter of the gyrus rectus (GR) and in front of the CN and anterior perforated substance (APS); arrows indicate the pathway. LV indicates lateral ventricle; gCC, genu of the corpus callosum; and OT, olfactory tract. Scale bar indicates 5 mm. (**B**) A montage of PCNA labeling of the human RMS shows the presence of numerous proliferating cells in both descending and rostral limbs of the RMS. Scale bar, 5 mm. (**C**) Schematic diagram demonstrating the pathway of the RMS as viewed laterally. (**D**) Diagram demonstrating the RMS from a frontal-oblique angle where the wide dorsal descending limb (DL) of the RMS descends and narrows to form the rostral limb (RL), which enters and courses rostrally in the OT toward the OB. (**E**) High-magnification photomicrograph of the PCNA-positive cells in the funnel part of the RMS. The area the photo was taken from is highlighted with a red box in (B). Scale bar, 50 μm. (**F**) Photomicrograph of the PCNA-positive cells in the DL of the RMS. The area the photo was taken from is highlighted with a red box in (B). Scale bar, 15 μm. (**G**) Photomicrograph of the PCNA-positive cells in the funnel part of the RMS. The area the photo was taken from is highlighted with a red box in (B). Scale bar, 30 μm.

cells were present. In the SVZ, the cell bodies faced the ependymal layer, and the processes were oriented away from the ependymal layer. The cell bodies were about 10 to 15 μm in diameter, and the length of the processes was half the width of the SVZ (Fig. 3, A to D). The gap region showed substantial background labeling and some small fiber staining (Fig. 3A). In the descending limb and the rostral limb of the RMS, there were also numerous bipolar and elongated PSA-NCAM–positive cells (Fig. 3, E to G). The olfactory tract core and periphery were also abundant in PSA-NCAM–positive cells that had a morphology and a staining pattern similar to those seen in the descending limb (Fig. 3, H and I). PSA-NCAM–positive cells in the OB were more randomly oriented, had fewer processes, and were larger than the cells in the olfactory tract core, indicating possible early stages of maturation (Fig. 3I). The descending limb had the largest number of PSA-NCAM–positive cells (the most PCNA cells were also present) within the RMS; the cell body labeling was mainly confined to a discrete bundle of bipolar cells (which showed leading and trailing processes) between the white matter of the gyrus rectus and the CN (Fig. 3E). In addition, small numbers of scattered PSA-NCAM–positive cells were seen just outside the main bundle, coursing into the surrounding white matter. In the rostral limb of the RMS, the morphology of the PSA-NCAM cells was similar to the morphology of those in the descending limb (Fig. 3, E and F). βIII-tubulin, an immature neuronal marker, was examined in the SVZ, the descending limb, and the olfactory tract. Fiber staining was observed in the SVZ beneath the gap region and close to the SVZ, as well as in the descending limb of the RMS (Fig. 4, A to C). In the descending limb, the fibers were particularly long and discretely located in the same place that PCNA immunoreactivity was located (Fig. 3, B and C). We performed double labeling and laser scanning confocal microscopy for PSA-NCAM and βIII-tubulin, which demonstrated that in the SVZ PSA-NCAM and βIII-tubulin are colocalized on the same bipolar cells (Fig. 4, D to F). Double-labeled PSA-NCAM– and βIII-tubulin–positive cells were seen in the olfactory tract (Fig. 4, G to J), as well as in the OB.

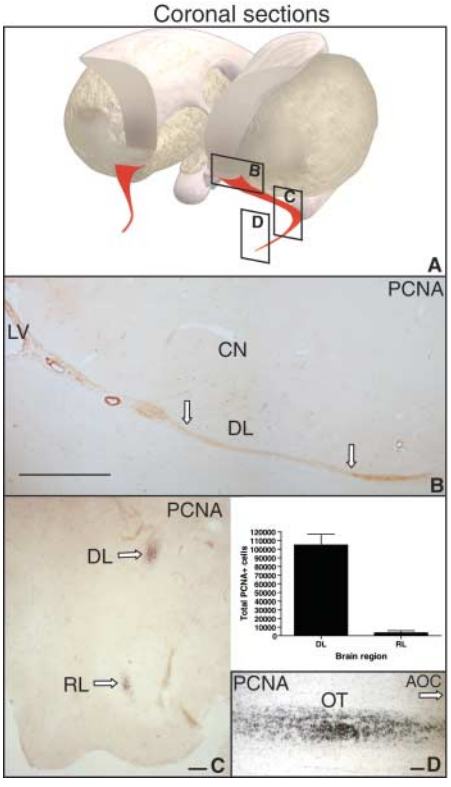

Fig. 2. The dorsal RMS is a broad band of proliferating cells, but ventrally there are fewer cells in the RMS. (**A**) Schematic diagram showing the orientation and location in the RMS of photomicrographs (B) to (D). (**B**) PCNA labeling in a montage of coronal serial forebrain sections showing the DL (arrows) as it courses laterally from the SVZ, then ventral to the CN. Scale bar, 1 mm. (**C**) PCNA labeling in a coronal section of the ventral forebrain showing a cross section of the DL (arrow) and the RL (arrow) of the RMS. The graph shows the total number of PCNA-positive cells in the RL compared with that of the DL of the RMS (n = 3). Scale bar, 200 μm. Error bars indicate SEM. (**D**) A longitudinal section of the OT very close to the AOC, showing large numbers of PCNA-positive cells. Scale bar, 100 μm.

Ultrastructural studies verify that the human SVZ contains cells with migratory-like morphology. In the adult mouse brain, where neuronal migration from the SVZ is common, ultrastructural and immunolabeling studies demonstrated that migrating neuronal precursors in the SVZ express PSA-NCAM (Doetsch classification, type A cells) (*6*, *7*). We sought to determine whether the human SVZ had similar migratory, type A cells. Electron microscopy (EM) revealed different types of cells that could be identified on the basis of their nuclear morphology and overall shape (Fig. 4K). Type A cells had an elongated cell body and a smooth contour. Their nuclei contained lax chromatin with one or two small nucleoli. They were located between the myelin layer and the ependymal layer. Positioned at the interface of the SVZ and myelin layer were the type B1 cells. These cells contained irregular nuclei with frequent invaginations and clumped chromatin [see (*8*) for a detailed analysis of type A, B, and C cells in the human SVZ]. We also detected an astrocytic ribbon in the SVZ of the adult human brain that contained dividing astrocytes (fig. S2), confirming previous work (*4*).

Progenitor cells become neurons in the OB. We used human OB from patients that had been administered 5-bromo-2′-deoxyuridine (BrdU) for the purpose of tracing the development of laryngeal and pharyngeal carcinomas. BrdU is a thymidine analog and labels cells in the S phase of the cell cycle (*9*, *10*). We double-labeled the OB with neuronal nuclei (NeuN), a mature neuronal marker, and an antibody against BrdU. Laser-scanning confocal z-series analysis revealed the colocalization of BrdU and NeuN in the same cells in the periglomerular layer (Fig. 4L), confirming previous work (*11*).

The human RMS is organized around a tubular extension of the lateral ventricle that reaches the OB. We performed gross dissection of the OB that revealed that the rostral OB region contains a hollow ventricle (Fig. 5, A and B). At the light microscope level, the wall of the olfactory ventricle was a scant layer of cells, although some of the cells were aligned in an ependymal-like layer (Fig. 5C). Ultrastructural analysis also revealed a loose cell structure in the wall of the olfactory ventricle; cells in the wall of the ventricle were nonciliated. The core of the olfactory tract also contained a hollow tube with predominantly acellular walls and associated blood vessels (Fig. 5D). Immunohistochemistry for PCNA at various anatomical planes of the descending limb of the RMS also revealed the RMS to be organized around a hollow tubelike structure (Fig. 5E).

By using magnetic resonance imaging (MRI) scans, we observed a central high signal consistent with fluid in the center of the OB. Surrounding the central core there was low-signal (black) OB tissue that was in the shape of the OB overlying the cribriform plate (Fig. 5, F to H). The visualized (with MRI) olfactory ventricle measured about 7 mm in length (Fig. 5, F and G), with a transverse diameter of about 1.5 mm (Fig. 5H).

Ultrastructural studies reveal progenitors at all levels of the RMS that have migratory morphology. Next, we wanted to determine the cell types present in the human VONS compared with the rodent brain, focusing on the OB, the olfactory tract, and the AOC with light microscopy (LM) and transmission electron microscopy (TEM). Figure 6A shows the location of samples for TEM and LM examination. In the OB on the ventral side, there were numerous large glomerular structures that had a prominent nerve fiber with multiple smaller branches and abundant synapses (Fig. 6, B and C). In the core region of the OB, caudal to the olfactory ventricle, a large number of progenitor-like cells were observed that had round nuclei and widespread euchromatin. These cells tended to be clustered in comparison with the mature cells in the OB that had irregularly shaped nuclei and predominantly heterochromatin (Fig. 6, D to G). The olfactory tract also contained numerous round progenitor cells that often appeared in groups (Fig. 6H). LM and TEM examination of longitudinal olfactory tract sections revealed groups of cells with elongated nuclei that were always oriented in the long axis of the olfactory tract (Fig. 6, I to K). In longitudinal sections, the cells often overlapped each other (Fig. 6I), and the leading end of the cells was usually prominent and for the most part free of organelles (Fig. 6J). EM of the longitudinally cut

tract revealed that progenitor cells had a pointed, narrow leading process that contained a few mitochondria, whereas the trailing area of the cell was densely packed with cell organelles and was much wider than the leading process (Fig. 6K). In the AOC, progenitor cells were present in a single layer (Fig. 6L). Collectively, progenitor cells in the RMS share some ultrastructural features with cells undergoing chain migration in the rodent RMS

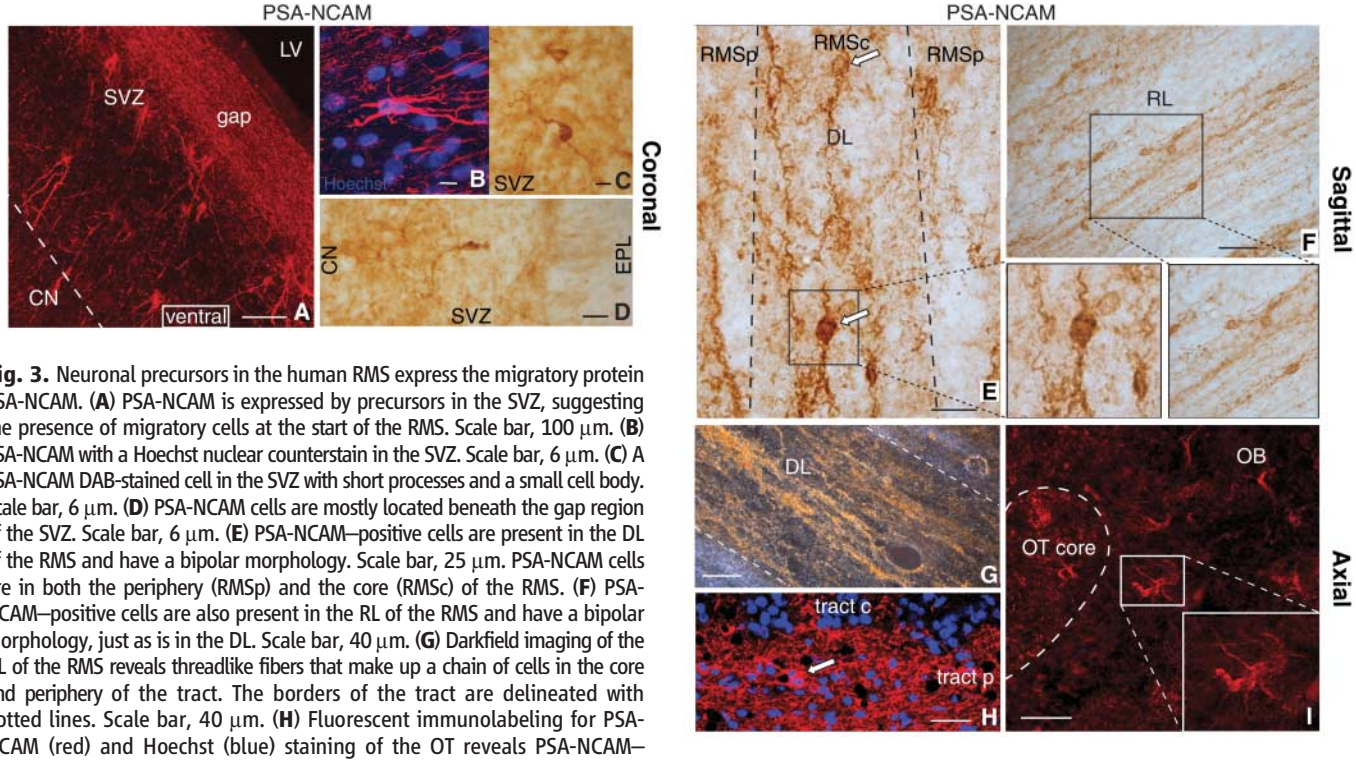

Fig. 3. Neuronal precursors in the human RMS express the migratory protein PSA-NCAM. (**A**) PSA-NCAM is expressed by precursors in the SVZ, suggesting the presence of migratory cells at the start of the RMS. Scale bar, 100 μm. (**B**) PSA-NCAM with a Hoechst nuclear counterstain in the SVZ. Scale bar, 6 μm. (**C**) A PSA-NCAM DAB-stained cell in the SVZ with short processes and a small cell body. Scale bar, 6 μm. (**D**) PSA-NCAM cells are mostly located beneath the gap region of the SVZ. Scale bar, 6 μm. (**E**) PSA-NCAM–positive cells are present in the DL of the RMS and have a bipolar morphology. Scale bar, 25 μm. PSA-NCAM cells are in both the periphery (RMSp) and the core (RMSc) of the RMS. (**F**) PSA-NCAM–positive cells are also present in the RL of the RMS and have a bipolar morphology, just as is in the DL. Scale bar, 40 μm. (**G**) Darkfield imaging of the DL of the RMS reveals threadlike fibers that make up a chain of cells in the core and periphery of the tract. The borders of the tract are delineated with dotted lines. Scale bar, 40 μm. (**H**) Fluorescent immunolabeling for PSA-NCAM (red) and Hoechst (blue) staining of the OT reveals PSA-NCAM–positive cells in the OT periphery (tract p, arrow). Scale bar, 25 μm. (**I**) The OT core and the OB have many PSA-NCAM–positive cells; in the bulb, the cells are more randomly oriented and larger than in the tract, suggesting early stages of maturation (high-magnification inset). Scale bar, 40 μm.

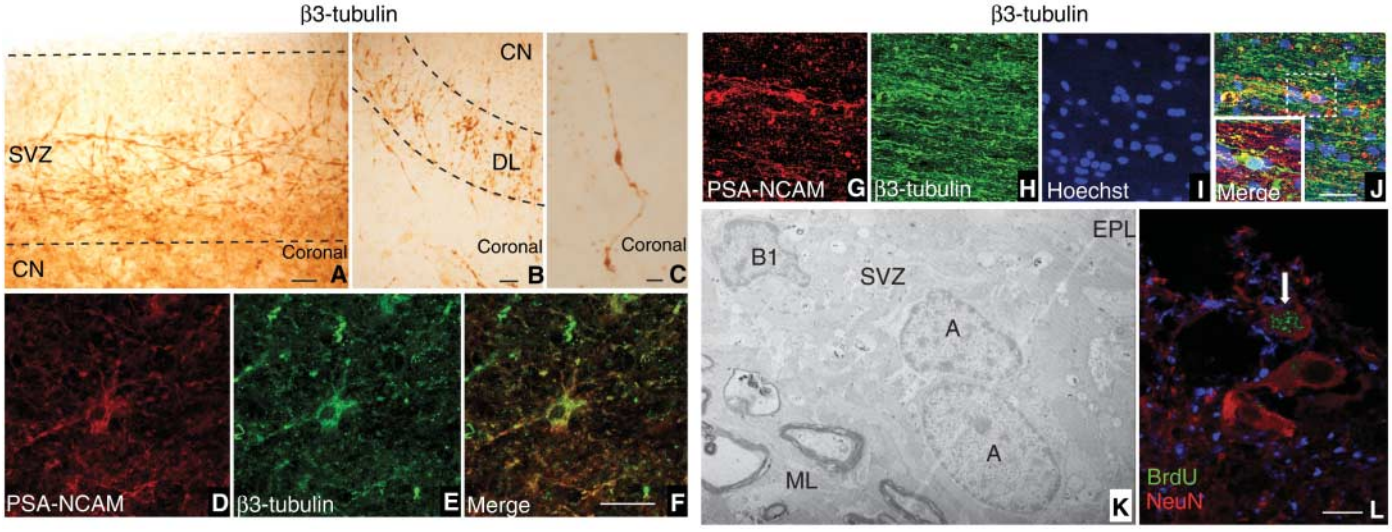

Fig. 4. Immature neurons that express both βIII-tubulin and PSA-NCAM are present in the RMS, and some mature in the olfactory bulb and express NeuN. (**A**) The immature neuronol marker βIII-tubulin forms a meshwork in the SVZ beneath the gap region. Scale bar, 20 μm. (**B**) The DL of the RMS has a bundle of βIII-tubulin fibers that follow the same path as the PSA-NCAM–positive cells. Scale bar, 20 μm. (**C**) High magnification of a βIII-tubulin–positive cell that reveals a cell body and two long processes that are oriented along the long axis of the DL of the RMS. Scale bar, 10 μm. (**D**) PSA-NCAM and (**E**) βIII-tubulin are colocalized in the same cell in the SVZ, as evidenced by the merged picture in (**F**). Scale bar, 20 μm. In the OT, (**G**) PSA-NCAM, (**H**) βIII-tubulin, and (**I**) Hoechst are colocalized (**J**) in the same cell in the periphery of the tract. Scale bar, 25 μm. (**K**) The rodent SVZ is enriched in type A cells that have an ultrastructure corresponding to the PSA-NCAM–positive cells that migrate in the RMS. This is an electron photomicrograph of cells in the human SVZ. Type A cells had an elongated cell body and smooth contour. Their nuclei contained lax chromatin with one or two small nucleoli. They were located between the myelin layer (ML) and ependymal layer (EPL). Positioned at the interface of the SVZ and myelin layer were type B1 cells. These cells contained irregular nuclei with frequent invaginations and clumped chromatin. (**L**) A cell expressing the mature neuronal marker NeuN (red) and the thymidine analog BrdU (green), indicating that adult-born neurons exist in the OB. Scale bar, 10 μm.

(*7*). Furthermore, immuno-TEM revealed that the cells with a migratory-like morphology were also positive for PSA-NCAM (fig. S3). There was an electron-dense cell membrane as a result of the PSA-NCAM contrasting; furthermore, there were many contrasted processes showing immunopositivity for PSA-NCAM (fig. S3). In the AOC, the progenitor cells were plentiful and tightly packed together with myelinated nerve fibers and mature cells.

Pax6, Olig 2, and DCX gene expression is consistent with differentiation along the VONS. Next, we investigated the differential gene expression pattern in different parts of the olfactory system. We performed reverse transcription polymerase chain reaction (RT-PCR) on fresh human brain homogenates from the AOC, the olfactory tract, and the OB. We chose to examine messenger RNA (mRNA) for three factors that regulate differentiation of olfactory neurons: Pax6, which induces differentiation; Olig2, which inhibits differentiation; and double cortin (DCX), which promotes cell migration (Fig. 6, M and N). Glyceraldehyde-3-phosphate dehydrogenase (GAPDH) was used as an internal control (*12*–*14*). As expected, Pax6 was highly expressed in the OB and weakly expressed in the AOC and the olfactory tract (Fig. 6M). This is consistent with previous studies showing the importance of Pax6 for the fate specification of progenitor cells into periglomerular neurons in the OB (*12*). In contrast, expression of Olig2, a transcription factor thought to inhibit olfactory neuron differentiation, was much higher in the olfactory tract compared with in the OB (Fig. 6M). RT-PCR for DCX revealed extensive expression in each region of the VONS examined, although the expression was higher in the OB than in the olfactory tract and the AOC (Fig. 6M). In the rodent brain, DCX is expressed throughout the olfactory system by progenitor cells that are migrating from the SVZ toward the OB (*15*). Therefore, it is not surprising that we see DCX mRNA evenly abundant in all regions of the VONS in the human brain. To confirm the PCR results, we immunostained various parts of the VONS with antibodies to Pax6, Olig2, and DCX (fig. S4).

Our work demonstrates a remarkable similarity between human and rodent olfactory systems. However, because of the pronounced enlargement of the frontal cortex in the human forebrain, most of the rostral CN, SVZ, and frontal cortex are located at levels rostral to the olfactory tubercle. The RMS in the human brain must, therefore, take a caudal path before entering the olfactory tract. In fact, forward rotation of the rodent forebrain by about 75° shows the RMS to be situated in an orientation comparable to that of the human; the larger frontal cortex and relatively smaller OB in the human accounts for this geometric difference between the human and the rodent RMS. Because the human RMS is relatively small and takes a caudal path before entering the olfactory tract (Fig. 1C), rigorous serial sagittal sectioning of whole forebrains was required to see the long axis of it (for example, Fig. 1A versus Fig. 2C). Previous attempts to find a human RMS (*16*) were probably unsuccessful because of the use of coronal sections in these studies. Our group has the access to large numbers of normal, well-preserved, perfused, whole human brains that was necessary for this extensive analysis of the VONS.

The VONS contains an extension of the lateral ventricle, the ventriculo-olfactory extension (VOE), that appears to be fluid-filled and is connected via a patent duct to the OB in the ventral forebrain. Thus, it appears that the human brain contains a continuous SVZ organized around the VOE that connects the lateral and the olfactory ventricles. The organization of the RMS around the VOE could support the notion that the migration of neuroblasts may be influenced by CSF circulation, as recently suggested (*17*).

Progenitor cells in the human VONS express PSA-NCAM and DCX, two proteins important for cell migration in the rodent RMS (*18*–*20*). These cells have many ultrastructural characteristics that have previously been used as reliable indicators of neuroblast migration in the rodent RMS (*17*, *21*). The close association of the progenitor cells to one another suggests that the progenitors may migrate in chains, as in rodents; alternatively, the progenitors may use the extracellular matrix surrounding the VOE (*21*). On the basis of the morphological characteristics of cells within the human VONS, the expression of migratory proteins, the orientation of the leading processes in the direction of migration, and the emergence of new neurons in the OB, we conclude that the cells within the human VONS probably undergo directed migration toward the OB. Studies in higher mammals have established that insults to the brain can induce neurogenesis via the recruitment of progenitor cells from the RMS (*22*). Our study

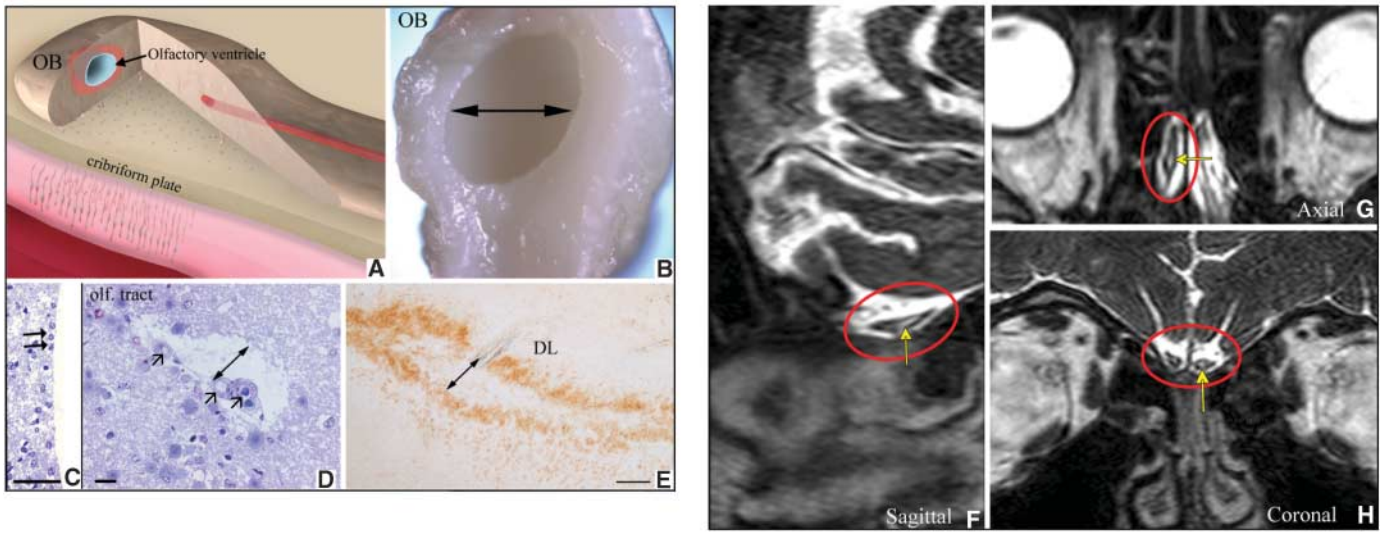

Fig. 5. The OB contains a hollow CSF-filled ventricle. (**A**) Diagram showing the hollow OB and part of the human olfactory sytem. (**B**) Dissections of the human OB reveal a hollow OB. The double arrow indicates the width of the olfactory ventricle. (**C**) LM of thin Richardson-stained sections showing unciliated, loosely packed cells in the olfactory ventricle wall (arrows). Scale bar, 100 μm. (**D**) Cross sections of the OT core reveal a hollow tube (double arrow). Blood vessels are indicated by single arrows. Scale bar, 10 μm. (**E**) A coronal, PCNA-stained section reveals a tubelike structure (double arrow) in the DL of the human RMS. Scale bar, 50 μm. (**F**) Sagittal, high-resolution heavily T2-weighted MR images of the rostral part of the human forebrain reveal that the elongated olfactory ventricle is in fact fluid-filled (arrow and red ring around the OB). (**G**) Axial MR image demonstrates fluid in the OB ventricle (red ring around the OB and arrow pointing to the central fluid compartment). (**H**) Coronal MR image shows two small fluid-filled compartments, one in each OB (red ring around the OB and arrow indicating the central fluid compartment).

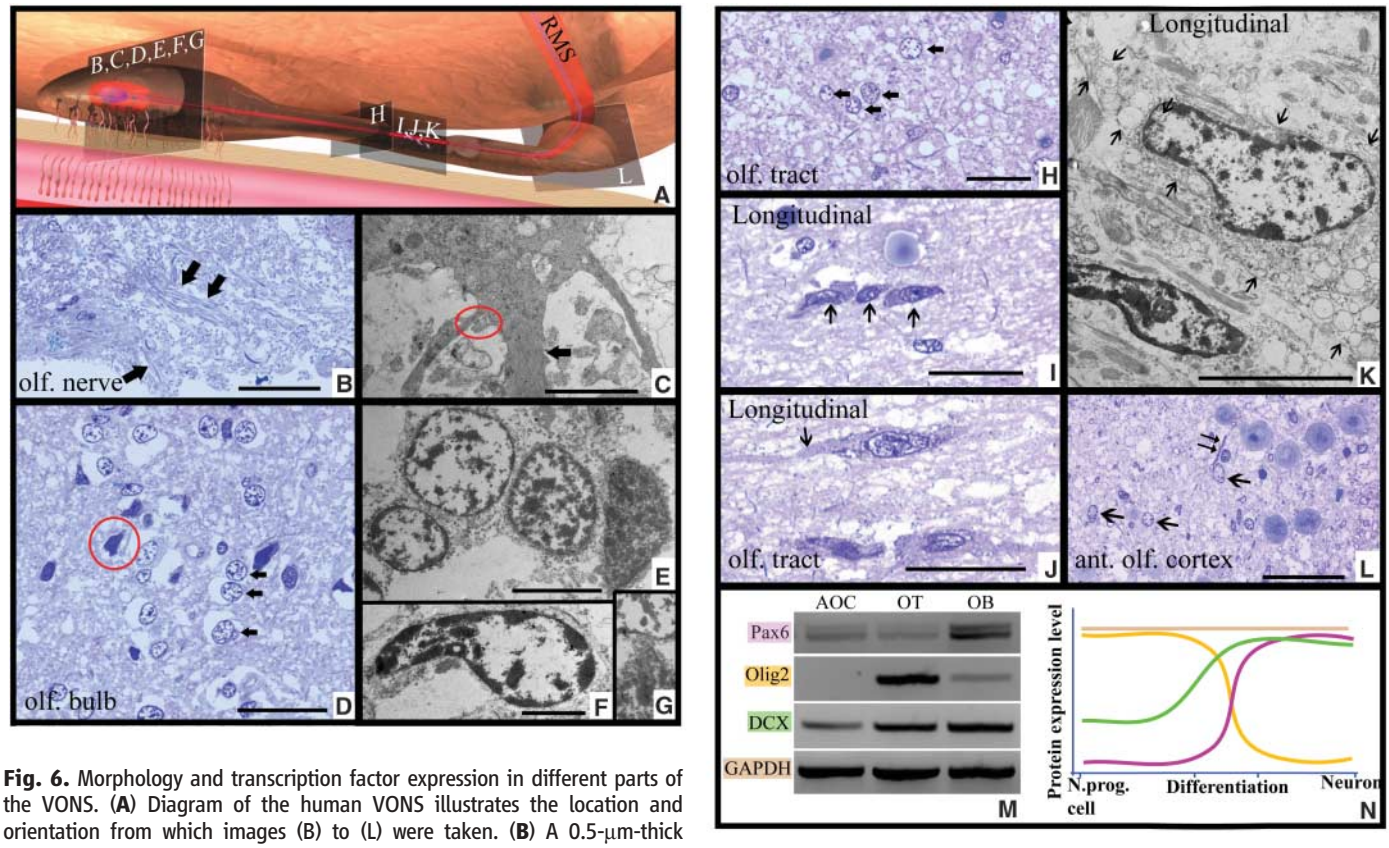

Fig. 6. Morphology and transcription factor expression in different parts of the VONS. (**A**) Diagram of the human VONS illustrates the location and orientation from which images (B) to (L) were taken. (**B**) A 0.5-μm-thick Richardson-stained section of the olfactory nerve fibers (arrows) in the OB. Scale bar, 100 μm. (**C**) Fibers of an olfactory nerve close to the surface of the OB (arrow) and a synapse with another nerve fiber (red ring). Scale bar, 2 μm. (**D**) The central region of the OB core contains progenitors (arrows) and more mature cells with irregularly shaped and densely stained nuclei (red ring). Scale bar, 100 μm. (**E**) Progenitor cells (three cells to the left) with aligned euchromatin and a mature cell (right) with heterochromatin and an irregular nucleus. Scale bar, 5 μm. (**F**) A mature cell with dense chromatin and an irregular nucleus, features of type B2 astrocytic cells. Scale bar, 2 μm. (**G**) The interface between an active (young) cell and an inactive (old/heterochromatin) cell is made clear by the nuclear density. (**H**) The OT contains round progenitor cells (arrows) that appear to be clustered together. Scale bar, 25 μm. (**I**) Progenitor cells with migratory features: elongated cell bodies and nuclei close to each other, with the leading process of one progenitor overlapping another progenitor (arrows). Scale bar, 25 μm. (**J**) A long leading process on a progenitor cell in the OT (arrow). The nucleus is elongated in the direction of the tract. Scale bar, 25 μm. (**K**) The ultrastructure of an elongated progenitor cell. The cells have an oval-shaped nucleus (in this plane), and cytoplasmic organelles are mostly located in the thickened trailing component of the cell (arrows indicate the cell membrane). Scale bar, 5 μm. (**L**) The AOC has many nerve fibers (parallel pair of arrows). The progenitor cells are present in one layer (single arrows). Scale bar, 100 μm. (**M**) Pax6 mRNA is highly expressed in the OB but not in the AOC or the OT. Olig2 is highly expressed in the OT and weakly expressed in the OB. DCX mRNA is expressed in AOC, OT, and OB. The housekeeping gene GAPDH is expressed equally in each region examined. (**N**) Scheme illustrating the relative abundance of Pax 6, Olig2, and DCX during the differentiation of progenitor cells.

provides a foundation for this possibility in the adult human brain.

The olfactory system has evolved as an important survival system to detect signs of danger such as smoke or contaminated food. The addition of new neurons in the human OB in adulthood may contribute to plasticity in this system. In rodents, the turnover of neurons in the adult OB is regulated by experience and modulates the circuitry in response to external stimuli. Some indications on the functional role of adult OB neurogenesis in humans may be gained from pathological conditions. Progenitor proliferation in the SVZ and neuroblast migration is reduced both in animal models and in patients with Parkinson's disease (*23*, *24*). Reduced OB neurogenesis in rodents results in impaired odor discrimination (*25*), a common and early sign of Parkinson's disease in humans. The presence, but also the function, of adult neurogenesis may be conserved from lower mammals to humans.

References and Notes

1. Brain Atlas of the Domestic Rabbit, www.brainmuseum.org/Specimens/lagomorpha/domesticrabbit/sections/thumbnail.html.
2. A. S. Rae, *Clin. Neuropathol.* **13**, 17 (1994).
3. G. Tomasevic, F. Kamme, T. Wieloch, *Mol. Brain Res.* **60**, 168 (1998).
4. A. Bedard, M. Levesque, P. J. Bernier, A. Parent, *Eur. J. Neurosci.* **16**, 1917 (2002).
5. L. Bonfanti, *Prog. Neurobiol.* **80**, 129 (2006).
6. F. Doetsch, J. M. Garcia-Verdugo, A. Alvarez-Buylla, *J. Neurosci.* **17**, 5046 (1997).
7. C. Lois, J. M. Garcia-Verdugo, A. Alvarez-Buylla, *Science* **271**, 978 (1996).
8. M. A. Curtis, H. J. Waldvogel, B. Synek, R. L. Faull, *J. Chem. Neuroanat.* **30**, 55 (2005).
9. F. Dolbeare, *Histochem. J.* **27**, 339 (1995).
10. F. Dolbeare, *Histochem. J.* **28**, 531 (1996).
11. A. Bernard, A. Parent, *Dev. Brain Res.* **19**, 159 (2004).
12. M. A. Hack *et al.*, *Nat. Neurosci.* **8**, 865 (2005).
13. M. Kohwi, N. Osumi, J. L. Rubenstein, A. Alvarez-Buylla, *J. Neurosci.* **25**, 6997 (2005).
14. A. Lee *et al.*, *Ann. Neurol.* **53**, 668 (2003).
15. J. P. Brown *et al.*, *J. Comp. Neurol.* **467**, 1 (2003).
16. N. Sanai *et al.*, *Nature* **427**, 740 (2004).
17. K. Sawamoto *et al.*, *Science* **311**, 629 (2006); published online 11 January 2006 (10.1126/science.1119133).
18. G. Chazal, P. Durbec, A. Jankovski, G. Rougon, H. Cremer, *J. Neurosci.* **20**, 1446 (2000).
19. H. Koizumi *et al.*, *Nat. Neurosci.* **9**, 779 (2006).
20. P. J. Ocbina, M. L. Dizon, L. Shin, F. G. Szele, *Mol. Cell. Neurosci.* **33**, 126 (2006).
21. B. T. Schaar, S. K. McConnell, *Proc. Natl. Acad. Sci. U.S.A.* **102**, 13652 (2005).
22. A. Arvidsson *et al.*, *Nat. Med.* **8**, 963 (2002).
23. G. U. Höglinger *et al.*, *Nat. Neurosci.* **7**, 726 (2004).
24. N. Freundlieb *et al.*, *J. Neurosci.* **26**, 2321 (2006).
25. P. M. Lledo, M. Alonso, M. S. Grubb, *Nat. Rev. Neurosci.* **7**, 179 (2006).

26. We thank J. F. Westin for assistance with the illustrations; G. Rougon for donation of the PSA-NCAM antibody; the Neurological Foundation of New Zealand for their support of M.A.C. as a Wrightson Postdoctoral Fellow and M.K. as a Miller Postgraduate Scholar; Swedish Medical Research

Council (project nos. 12X-1253 and K2002X-72X-10358-10A); Swedish Cancer Research Foundation (project no. 3911); Torsten och Ragnar Söderbergs Foundation; King Gustaf V:s and Drottning Victorias Foundation; Axel Linders Foundation; the Regional Developmental Board and the Chamber of Commerce and Industry in Western Sweden; Sahlgrenska Academy; the Neurological Foundation of New Zealand; the Health Research Council of New Zealand; the National Research Centre for Growth and Development, New Zealand; A.-M. Alborn, and J. Lind for the technical support; and J. Faijerson, M. Komitova, and G. Kuhn for scientific and technical advice.

Supporting Online Material

www.sciencemag.org/cgi/content/full/1136281/DC1
Materials and Methods
Figs. S1 to S5
Table S1

13 October 2006; accepted 24 January 2007
Published online 15 February 2007;
10.1126/science1136281
Include this information when citing this paper.

REPORTS

Predictions of the Properties of Water from First Principles

Robert Bukowski,[1] Krzysztof Szalewicz,[1] Gerrit C. Groenenboom,[2] Ad van der Avoird[2]

A force field for water has been developed entirely from first principles, without any fitting to experimental data. It contains both pairwise and many-body interactions. This force field predicts the properties of the water dimer and of liquid water in excellent agreement with experiments, a previously elusive objective. Precise knowledge of the intermolecular interactions in water will facilitate a better understanding of this ubiquitous substance.

Water has been extensively studied on account of its ubiquity and importance for so many aspects of human activity. The deceptively simple water molecule forms one of the most complex liquids and solids, and investigations continue to focus on all forms of pure water, including small clusters [e.g., (*1*, *2*)], bulk liquid [e.g., (*3*–*6*)], and a multitude of ice polymorphs. Similarly numerous are theoretical analyses of water, all of which require knowledge of the intermolecular potential (the derivatives of this potential give the force field that governs the dynamics). Most such investigations use empirical pair potentials fitted to reproduce certain measured bulk properties in Monte Carlo (MC) or molecular dynamics (MD) simulations of water. These "effective" potentials account for the important many-body interactions in water by (nonphysical) deformations of the true pair potential. The well-known result is that such potentials poorly describe the water dimer, give very inaccurate second virial coefficients, and fail to reproduce experimental spectra of small water clusters. Therefore, studies of molecular-scale properties of water with empirical potentials, such as the molecular jump mechanism of water reorientation (*7*), may suffer from an inadequate representation of the force field. Another known drawback of empirical potentials is that the quality of their predictions deteriorates quickly beyond the range of thermodynamic parameters used in the fitting procedure. Moreover, there does not appear to be any systematic method to improve the predictive accuracy of these potentials.

Another way of obtaining the force fields—which does not require prior knowledge of any experimental data—is by quantum mechanical ab initio calculations. Such an approach can provide the most reliable foundation for an understanding of water and other substances. However, the accuracy of ab initio force fields is limited by unavoidable approximations in the level of theory and incompleteness of basis sets.

A first-principles approach can proceed either "on the fly" (i.e., by computing the electronic energy for each configuration of the N molecules present in a simulation of bulk water, where N at least equals 32) or by computing the interaction energy as a sum of relatively simple analytic many-body potentials (pair, three-body, etc.) fitted beforehand to ab initio data. The former approach can be realized only with the fastest electronic structure methods such as density functional theory (DFT). Although for some time the published results suggested that this approach reproduced the properties of liquid water very well, recent work has shown that this agreement was due to fortuitous choices of the DFT functionals (*8*). Even for the same functional, different values of some parameters in the simulations may lead to markedly different predictions [e.g., the results in (*9*) and (*10*)]. Moreover, the current DFT approaches cannot describe the dispersion component of the intermolecular interaction energy, which is nonnegligible in water.

The many-body expansion of the potential requires ab initio calculations on dimers, trimers, and larger clusters. If the many-body expansion converges sufficiently rapidly, such calculations can be restricted to only a few small clusters and can make use of accurate electronic structure methods. In practice, the interaction energy must already be well reproduced at the three-body level, because calculations of the complete four-body potential for water would be too time-consuming. An important advantage of using the many-body expansion approach is that it can be systematically improved by extending the level of theory, using larger basis sets, calculating more grid points, and improving the form of the fitting function. A large number of ab initio water dimer potentials have been published [e.g., (*11*–*16*)]. However, so far no first-principles approach has simultaneously reproduced the experimental results for both the water dimer and the condensed phases of water. Here we present substantial progress toward this goal.

We developed a pair potential for water on the basis of the coupled cluster method with single, double, and noniterative triple excitations [CCSD(T)], generally regarded as the most accurate of practically applicable electronic structure methods. We have used the same set of 2510 carefully selected grid points as in the SAPT-5s potential developed previously by our group (*12*). The H_2O monomer was assumed to be rigid in the averaged ground-state vibrational geometry, as in (*12*). For each grid point, we first computed the interaction energies with the use of second-order perturbation theory based on the Møller-Plesset partitioning of the Hamiltonian (MP2). The MP2 energies were computed in augmented triple- and quadruple-zeta quality basis sets supplemented by midbond functions. The energies were then extrapolated to the complete basis set (CBS) limit by means of the well-established extrapolation formula that assumes a convergence rate proportional to the inverse third power of the cardinal number of the basis set. The CCSD(T) contribution beyond the MP2 level was computed in the triple-zeta quality basis set and added to the extrapolated MP2 values. We also performed single-point calculations in a quintuple-zeta quality basis. The basis set convergence patterns indicate that the uncertainty of the computed interaction energies is about 0.07 kcal/mol. For comparison, the uncertainty of the SAPT-5s potential was 0.3 kcal/mol. The accuracy of the current calculations is virtually the same as that of the most extensive published ab initio work [e.g., (*17*)]. However, the cited calculations have been performed only for a few selected geometries of the dimer, whereas we have obtained the complete six-dimensional potential surface.

[1]Department of Physics and Astronomy, University of Delaware, Newark, DE 19716, USA. [2]Theoretical Chemistry, Institute for Molecules and Materials, Radboud University Nijmegen, Toernooiveld 1, 6525 ED Nijmegen, Netherlands.